Next Nanotechnology 7 (2025) 100141

Contents lists available at ScienceDirect

Next Nanotechnology

journal homepage: www.sciencedirect.com/journal/next-nanotechnology

Research Article

Enhancing magnetic hyperthermia: Investigating iron oxide nanoparticle coating and stability

Joana Santos [a,b], Jorge Carvalho Silva [b], Manuel A. Valente [c], Tânia Vieira [b], Paula I.P. Soares [a,*]

[a] i3N/CENIMAT, Department of Materials Science, NOVA School of Science and Technology, NOVA University of Lisbon, Campus de Caparica, Caparica 2829-516, Portugal
[b] i3N/CENIMAT, Department of Physics, NOVA School of Science and Technology, NOVA University of Lisbon, Campus de Caparica, Caparica 2829-516, Portugal
[c] Physics Department (i3N), University of Aveiro, Campus Universitário de Santiago, Aveiro, Portugal

ARTICLE INFO

Keywords:
Protein corona
Superparamagnetic iron oxide nanoparticles
Magnetic hyperthermia
Nanotechnology
Stability

ABSTRACT

Cancer treatment research focuses on overcoming the limitations of conventional treatment methods, especially in addressing treatment-resistant malignancies. Magnetic hyperthermia (MH) is an innovative approach that uses superparamagnetic iron oxide nanoparticles (SPIONs) to increase the temperature locally, triggering cancer cell death. However, challenges related to the SPIONs coating impact their stability and MH heating mechanism, hindering its clinical adoption. This work explores diverse SPIONs coating options - oleic acid (OA), dimercaptosuccinic acid (DMSA), and (3-aminopropyl)triethoxysilane (APTES), to improve SPIONS stability under storage while keeping their heating capacity. OA- and DMSA-coated SPIONs, both negatively charged NPs, exhibited similar behavior in protein corona formation and MH tests. The heating capacity of the three types of SPIONs was maintained after 1 month of storage; however, these values significantly decreased to about 60 % of the initial value after 6 months. APTES-coated SPIONs displayed higher protein corona formation, mainly related to the positively charged surface. Interaction studies with three cell lines (fibroblasts, melanoma, and macrophages) revealed enhanced internalization of APTES-coated SPIONs. Only APTES-coated SPIONs achieved therapeutic temperatures in MH assays, reducing melanoma cell viability significantly. The study underscores the importance of nanoparticle surface modifications and the complexity of factors influencing treatment efficacy. Further research is essential for a better understanding of the cell death mechanism induced by MH and for its clinical translation.

1. Introduction

Nowadays, cancer treatment encompasses diverse methods, including local approaches like surgery and radiation therapy, along with systemic treatments such as chemotherapy, immunotherapy, and targeted therapy tailored to cancer type and stage. Despite these options, cancer remains a leading global cause of death. The 2020 statistics attribute almost 10 million deaths to this disease, which represents approximately one in six deaths, and projections predict that this figure will rise to 16.3 million in 2040 [1,2]. Treatments often yield side effects and may not halt disease progression [3]. Therefore, a method that is adaptable across cancer types, with high specificity for cancer cells, and minimal side effects is needed.

In recent years, nanotechnology has displayed significant potential, particularly in medicine. Specifically, the use of nanoparticles (NPs) has emerged as a strategy to increase the effectiveness of cancer treatments, namely in drug delivery and magnetic hyperthermia (MH) [4–6]. MH is an innovative therapy that employs superparamagnetic NPs subjected to alternating magnetic fields (AMF) to induce cell death through localized heat generation. This therapy gained prominence in nanomedicine for its advantageous aspects in effective antitumor treatment, including biosecurity, deep tissue penetration, radio-resistance reduction, and destruction of specific tumors [7,8]. However, significant challenges must be addressed for MH to fully exploit its potential as a viable alternative for cancer treatment.

In physiological environments, NPs usually lose stability, adsorb proteins, form the well-known protein corona (PC), and aggregate, which can strongly affect their properties [9,10]. To address this, NPs

* Corresponding author.
E-mail addresses: joanafsantos75@gmail.com (J. Santos), jcs@fct.unl.pt (J.C. Silva), ts.vieira@fct.unl.pt (T. Vieira), pi.soares@fct.unl.pt (P.I.P. Soares).

https://doi.org/10.1016/j.nxnano.2025.100141
Received 8 November 2024; Received in revised form 24 January 2025; Accepted 3 February 2025
Available online 5 February 2025

are typically coated with surfactants or other materials. Some examples of coating agents employed for surface modification of NPs include oleic acid (OA), dimercaptosuccinic acid (DMSA), and (3-aminopropyl) triethoxysilane (APTES). However, selecting the right stabilizing agent remains a significant challenge since it significantly impacts several critical factors, such as the "bio-identity" of NPs, stability in the physiological environment, and cellular interactions [11]. In addition, MH encompasses a broad spectrum of parameters that, when altered, can trigger different cell death pathways. This complexity contributes to the difficulty and inconclusive nature of research into understanding the various cell death mechanisms induced by MH therapy.

In superparamagnetic iron oxide nanoparticles (SPIONs), preventing aggregation is particularly important. Aggregated SPIONs lose their single-domain particle characteristics, compromising their superparamagnetic properties crucial for MH efficacy [12]. Guibert *et al.* [12] examined aggregation's impact on SPIONs' heating capacity, highlighting specific absorption rate (SAR) variation. They found that small aggregates resemble well-dispersed NPs in SAR and that large aggregates exhibit decreased heating efficiency, influenced by aggregate compactness. Coating agents affect protein adsorption, as observed by Calatayud *et al.* [13], who compared negatively and positively charged NPs' hydrodynamic sizes in biological media [11]. When evaluating the MH-induced cell death mechanism, there is a wide range of parameters that, when varied, lead to the activation of diverse cell death pathways, and this is reflected in the difficulties and lack of consensus observed in this field [14–17].

The main objective of the present work is to explore OA, DMSA, and APTES as coatings for SPIONs, assessing their stability, interactions with different cell types, and MH applications. These stabilizers were chosen based on two permisses: having a positive and negative surface charge and based on the research team's previous experience. We have previously demonstrated the effectiveness of both OA and DMSA as coating agents of iron oxide nanoparticles for magnetic hyperthermia applications [5,18–20]. However, the *in vitro* effects were still undiscovered. Therefore, we used these two negatively charged modifiers and APTES for a more comprehensive study. SPIONs stability, aggregation, and heating capacity during storage were evaluated. The interaction of coated SPIONs with different cell lines was also evaluated, providing novel insights into the effects of SPIONs coating on their interaction with cells and their efficacy as MH agents.

2. Materials and methods

2.1. Iron oxide nanoparticles synthesis

The synthesis of SPIONs was accomplished through a chemical co-precipitation technique adapted from the method described by Soares *et al.* [21]. The 1,10- phenanthroline colorimetric method was used to quantify the amount of iron in each SPIONs solution after synthesis [21,22]. Ultrapure water was purified in-house using a Milli-Q® Synthesis A10 Water Purification System connected to an Elix® Essential 10 UV Water Purification System from Merck Millipore (Madrid, Spain).

The procedures followed for stabilization with OA and DMSA are described in Soares *et al.* [21] and Fauconnier *et al.* [23], respectively. Briefly, after synthesis, SPIONs were washed with ultrapure water with the aid of a magnet. After measuring the final NP concentration, a known amount of OA (64 % of NP total mass) was added to the NP suspension. Regarding the DMSA stabilization, the solution's pH was adjusted to 3 using 65 % nitric acid (Panreac). DMSA (Acros Organics) was first dissolved in 2 mL of ultrapure water, and the pH was adjusted to 5.5 using a 0.1 M NaOH solution (EKA Chemicals) with vigorous stirring. Following this, DMSA (Acros Organics) was added at a ratio of 3:4 of [DMSA]/[Fe^{2+}]. After these steps, OA and DMSA-coated SPIONs were separately left to react for about 2.5 h in an ultrasound bath. Finally, the stabilized SPIONs were subjected to dialysis using a 12–14 kDa MWCO Dialysis Membrane Tube 4 RC (Spectrum™ Spectra/Por™) against ultrapure water until neutral pH.

The stabilization with APTES was carried out according to the method described by Mashhadizadeh *et al.* [24]. After settling, the SPIONs suspension was treated with a 10 % (v/v) APTES (Merck) and glycerol solution in a 1:2 ratio. The mixture reacted for 2 h at 90°C with stirring, followed by five washes with ultrapure water and ethanol upon cooling to room temperature.

2.2. Characterization

A UV–VIS spectrophotometer (PG Instruments model T90 +) quantified iron content in each SPIONs synthesis using a calibration curve derived from Mohr's salt solution in HCl 0.01 N (10–1000 μg mL^{-1}).

Fourier transform infrared (FTIR) spectroscopy, thermogravimetric analysis (TGA), X-ray diffraction (XRD), transmission electron microscopy (TEM), and dynamic light scattering (DLS) analyzed stabilized synthesized SPIONs. For FTIR, TGA, and XRD, freeze-dried SPIONs were used. FTIR spectra were obtained using a Nicolet 6700 (Thermo Electron Corporation) with attenuated total reflectance (ATR). Measurements were performed in the range of 480–4000 cm^{-1} with a resolution of 1 cm^{-1}. XRD analysis was performed with a Panalytical X'Pert PRO MDP X-ray diffractometer with Cu-Kα radiation (15° to 80°, 0.033° step). TGA measurements employed a TGA-DSC – STA 449 F3 Jupiter (heating rate of 10 °C/min, 25–900 °C, oxygen-free atmosphere). TEM images were obtained from diluted SPIONs solutions (0.5 μg mL^{-1}) on a 25 mesh Kevlar grid using a Hitachi H-8100 II with LaB6 thermionic emission. DLS analyzed the hydrodynamic diameter (D_H) of the SPIONs suspensions (0.025, 0.05, and 0.1 mg mL^{-1}) in ultrapure water (θ = 90°). ζ-potential was evaluated with a graphite electrode. All the DLS measurements were performed using a SZ-100 nanopartica series with a laser of 532 nm and controlling temperatures with a Peltier system (25 °C). The heating capacity of SPIONs was measured upon exposure to a magnetic field strength of 300 Gauss and a frequency of 388.4 kHz using an Nb Nanoscale Biomagnetics D5 equipment. The temperature of the sample was measured using an optical probe placed at the center of the sample. SAR was determined using Eq. 1 [18].

$$SAR = \frac{C_{NP}m_{Fe} + \quad C_1 m_1}{m_{Fe}} \left(\frac{dT}{dt}\right)_{\max} \tag{1}$$

Where C_{NP} is the specific heat of the SPIONs, C_1 is the specific heat of the liquid, m_1 is the mass of the fluid, m_{Fe} is the mass of iron in the colloid, and (dT/dt) max is the maximum gradient of the suspension temperature curve. Testing involved four concentrations (1, 2.5, 5, and 10 mg mL^{-1}) in ultrapure water, with a temperature stabilization interval followed by a 10 min field application using 1 mL of each sample. Magnetic properties of Fe_3O_4 NPs were measured through Vibrating Sample Magnetometer (VSM) technique using a 10 T VSM magnetometer (Cryogenic-Cryofree). The magnetization curve was obtained at 300 K, with a variation of the applied field of −2 T up to 2 T.

2.3. Protein corona formation

For this test, SPIONs with the three types of coatings were prepared at a concentration of 0.05 mg mL^{-1}, and different filtered (0.22 μm pore syringe) dispersion media were tested. The formation of PC was tested using ultrapure water and the three types of cell culture media appropriate for each cell line under study with and without fetal bovine serum (FBS, Biowest). After incubating the samples for 3 h, 6 h, 12 h, and 24 h, DLS was used to measure the protein corona of these samples in triplicates under the same conditions mentioned above. The media had pH values of about 7.0, 6.9, 7.4, 7.8, and 7.4 for ultrapure water, Phosphate-buffered saline (PBS), Roswell Park Memorial Institute 1640 (RPMI, Biowest), low glucose Dulbecco's Modified Eagle's Medium (DMEM-LG, Biowest), and high glucose Dulbecco's Modified Eagle's Medium

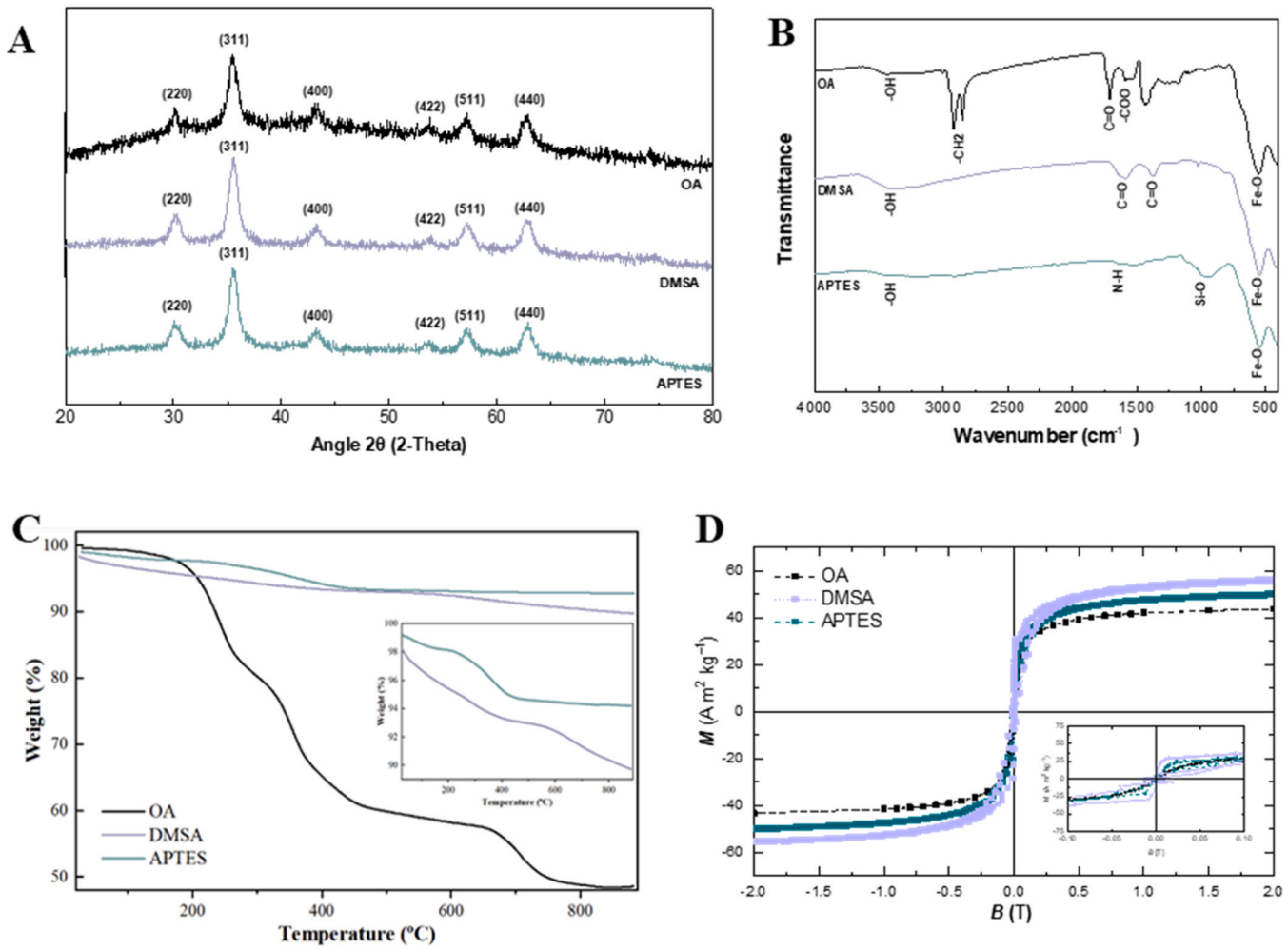

Fig. 1. X-ray pattern (A), FTIR spectra (B), TGA curves (C), and Magnetization as a function of the applied magnetic field at 300 K (D) of SPIONs synthesized by the chemical co-precipitation technique. SPIONs coated with OA (black line), DMSA (purple line,) and APTES (green line). Magnetization values are presented in Am^2 per kg of the whole particle (including magnetic and non-magnetic material).

(DMEM-HG, Biowest) respectively.

2.4. Cell culture

Three cell lines were used for the different assays: advanced cutaneous melanoma cancer cells WM983b (Rockland), human Caucasian fetal foreskin fibroblast cells HFFF2 (ECACC 86031405), and a human leukemia monocytic cell line THP-1 (ATCC TIB-202TM). WM938b cells were cultured in DMEM-HG supplemented with 1 % penicillin-streptomycin (P/S, Gibco) and 5 % heat-inactivated FBS. HFFF2 cells were grown in DMEM-LG supplemented with 1 % P/S and 10 % FBS. THP-1 cells were grown in RPMI medium supplemented with 1 % P/S, 10 % heat-inactivated FBS, 1 % sodium pyruvate, and 1 % non-essential amino acids (both from Gibco). All cell lines were maintained in an MCO-19AIC(UV) CO_2 incubator (Sanyo) with 5 % CO_2 at 37 °C.

2.5. Cytotoxicity assay

For the resazurin assay, WM983b, THP-1, and HFFF2 cells were seeded in 96-well plates at densities of 100k cell/mL, 600k cell/mL, and 90k cell/mL, respectively, and left to adhere for 24 h. In a culture medium, cells were exposed to various SPION concentrations (1 mg mL^{-1} to 0.0625 mg mL^{-1}) for 24 and 48 h. Positive control cells were cultured with a medium supplemented with 10 % DMSO while negative control cells were cultured with a complete medium. After incubation, wells were washed, and a solution containing 50 % culture medium supplemented with 50 % resazurin solution (0.04 mg mL^{-1} in PBS, Alfa Aesar) was added. After 3 h of incubation at 37 ºC and 5 % CO_2, absorbance was measured at 570 and 600 nm using a BioTek Elx800 UV microplate reader. Cell viability was calculated as [% cell viability = (cells treated with NPs/control cells) × 100].

2.6. Internalization study

The uptake of SPIONs by the three cell lines was assessed using Prussian blue staining. Cells were seeded in 24-well plates with coverslips, tripling the cell densities of the resazurin assay, and allowed to adhere for 24 h. They were then exposed to SPIONs for 1, 6, and 24 h at 100 μg mL^{-1}, with a control without NPs. Gentamicin (1:1000 from a stock solution of 10 mg mL^{-1}, Gibco) was added with the NPs. After each time point, cells were washed with PBS and fixed with 4 % paraformaldehyde (PFA, Sigma Aldrich). After washing, cells were treated with Perl reagent (Merck) for 40 min, washed again, and coverslips were mounted on slides using Mowiol mounting media (Sigma-Aldrich). Three replicates were prepared for each condition, and approximately 12 images were obtained per well using a Nikon Ti-S inverted microscope at 40x magnification.

2.7. In Vitro magnetic hyperthermia

For the in vitro MH assay, 500k cells/mL and 450k cells/mL of WM983b and HFFF2, respectively, were seeded in hyperthermia vials in a total volume of 1 mL and left to incubate for 24 h at 37ºC and 5 % CO_2. SPIONs were added at 5 mg mL^{-1} in the corresponding cell medium with gentamicin antibiotic (1:1000). After 24 h of further incubation, MH assays were conducted using a nB Nanoscale Biomagnetics D5 series apparatus with 1 mL samples. A 300 G AMF at 388.4 kHz was applied until reaching 45 °C or after 25 min. After MH treatment, each flask was rinsed 2x with the respective cell culture medium, and 500 μL of a 50 % resazurin solution (50 % resazurin plus 50 % complete medium) was added. Flasks were incubated at 37ºC and 5 % CO_2 for about 2 h to allow fluorescence without saturation. Resazurin solution was then transferred to a 96-well cell culture plate, 100 μL/well. After removal of the resazurin solution, each flask received 1 mL of cell culture medium with gentamicin (at a 1:1000 ratio from a 10 mg mL^{-1} stock solution) for a repeat resazurin assay after 24 h. The absorbance of the 96-well plate containing the resazurin solution was measured at 570 and 600 nm using a BioTek ELx800 UV absorbance microplate. Cell viability was calculated as [% cell viability = (test cells/incubator control cells) × 100].

2.8. Sand bath hyperthermia

The three cell lines were seeded separately in a 24-well plate for this assay, maintaining the cell density used for the resazurin assay. After the cells adhered, 500 μL of SPIONs coated with APTES at a concentration of 100 μg mL^{-1} were added, and the plate was incubated again for a period of 24 h. After this period, the plate was placed in a sand bath for 1 h at a 42–44 °C temperature range. Immediately after hyperthermia, a solution of resazurin (Alfa Aesar) with a concentration of 0.04 mg mL^{-1} was placed on the wells to get a final resazurin concentration of 0.02 mg mL^{-1}, and the plate was incubated again for a period of approximately 2h30 to avoid signal saturation. After this time, 100 μL of the solutions from each well were transferred to a non-sterile 96-well cell culture plate before reading to minimize any potential influence of the SPIONs' color on the absorbance values. The absorbance was then measured at 570 and 600 nm wavelength using the BioTek ELx800 UV absorbance microplate reader, and cell viability was expressed as a percentage of the control (plate that was not heated), given by [% cell viability = NP treated cells/control cells × 100]. After this, half of the replicates were fixed, and the other half were placed with 400 μL of the respective medium in each well and incubated again. For the fixation process, the cells were washed 4x with phosphate buffer saline (PBS), and 400 μL/well of 4 % paraformaldehyde (PFA, Sigma Aldrich) was added. After a period of about 15 min, the cells were washed 3x with PBS and then permeabilized with 400 μl 0.5 % Triton-X 100 for 20 min. After being washed with PBS, the cells were stained with ActinstainingTM 555 Phalloidin Red (Cytoskeleton) dissolved in 0.2 % PBS solution at 100 nM. Each coverslip was covered with 50 μl of the staining solution for 1h30min. Then, each coverslip was washed with PBS, and nuclear staining was performed by adding 50 μL of a 10 μM 4',6-diamino-2-phenylindone (DAPI, Molecular Probes) solution dissolved in the PBS solution and left to act for about 3–4 min. After this staining, the coverslips were washed with PBS and water and mounted on slides on 10 μl of Mowiol mounting medium (Sigma-Aldrich). The samples were visualized with an epi-fluorescence microscope Nikon Eclipse Ti-S.

3. Results and discussion

3.1. Physicochemical characterization

Employing diverse methodologies, the synthesized SPIONs underwent characterization encompassing chemical composition, morphology, size distribution, and magnetization analysis.

Fig. 1 A shows the XRD patterns obtained from the synthesized SPIONs coated with OA, DMSA, and APTES. The three patterns exhibit the presence of six distinctive 2θ peaks associated with these NPs, positioned at 30.3, 35.6, 43.3, 53.6, 57.2, and 63.1 degrees, corresponding to the diffraction planes (220), (311), (400), (422), (511), and (440), respectively [21]. XRD patterns resembling standard magnetite powders (JCPDS 00–019–0629), suggesting stabilizers do not affect SPIONs' crystal structure. Nevertheless, the presence of maghemite cannot be discarded as the standard XRD patterns (JCPDS 00–039–1346) are similar. In a previous study, Soares *et al.* [21] demonstrated that coating iron oxide nanoparticles with different surfactants (oleic acid, sodium citrate, and Triton X-100) do not alter the crystalline structure or size of these nanoparticles, which is in accordance with the presented findings.

Quantitative analysis of crystallinity showed average core diameters of approximately 7.9 nm, 6.8 nm, and 7.5 nm for OA, DMSA, and APTES-coated SPIONs, respectively, based on Scherrer's Eq. (2) [25]:

$$\tau = \frac{K\lambda}{\beta \cos\theta} \quad (2)$$

Fig. 1 B displays spectra obtained between 500 and 4000 cm^{-1}, revealing characteristic SPIONs bands: a strong absorption band at approximately 550 cm^{-1} (Fe-O stretching), a band at 1590 cm^{-1} (O-H stretching), and a broader band between 3000 and 3500 cm^{-1} (O-H stretching due to water) [8]. FTIR spectra of pure coating molecules (OA, DMSA, and APTES) are presented in Figure S1 of the Supplementary information. In the spectra of pure oleic acid, the sharp bands at 2853 and 2923 cm^{-1} are due to the symmetric and asymmetric stretching vibration of CH_2. The sharp band at 1708 cm^{-1} is related to the stretching vibration of C═O from the free carboxylic group. The O−H in-plane and out-of-plane vibration bands are present at 1646 and 937 cm^{-1}, respectively. The bending vibration of C−O group is present at 1283 cm^{-1} [26]. Regarding the FTIR spectrum of OA-coated SPIONs, the sharp bands at approximately 2920 and 2853 cm^{-1} represent the symmetric and asymmetric -CH_2 stretching in the OA molecule, respectively. The band at 1710 cm^{-1} corresponds to the C═O stretching vibration and indicates the formation of an OA bilayer. This bilayer is significant as it imparts hydrophilicity to the SPIONs, enhancing their stability in aqueous solutions. Additionally, bands at approximately 1590 and 1415 cm^{-1} can be attributed to the symmetric and asymmetric -COO stretching vibration modes, respectively, indicating covalent bonding between the -COO- groups of the OA and the Fe atom of SPIONs [8,21,26].

In the FTIR spectra of pure DMSA (Figure S1, Supplementary information), the characteristic band at 1688 cm^{-1} is related to the stretching vibration of the carbonyl group (C═O), while at 1179 cm^{-1} is due to the stretching vibration of C−O group. The bands confirm the presence of OH groups at 1418 cm^{-1} (in-plane deformation) and 924 cm^{-1} (out-of-plane deformation), characteristic of the carboxylic dimer. The S−H characteristic groups of DMSA are evidenced at 2536 and 2562 cm^{-1} (stretching vibrations of S−H) and 692 cm^{-1} (C−S stretching vibration). The aliphatic chain is evidenced by the bands present at 1289, 1312 cm^{-1} (deformation vibration of C−H), and 2835 cm^{-1} (symmetric stretching vibration of C−H) [27]. The FTIR spectrum of DMSA-coated SPIONs shows a lower intensity of the absorption bands, and the characteristic groups of DMSA are not clearly visible. The bands at approximately 1592 cm^{-1} and 1373 cm^{-1} indicate carboxylate groups' asymmetric and symmetric stretching. The band at 1011 cm^{-1} is attributed to the C−O ether stretch. Given the large splitting between the $-COO^-$ bands, the carboxylate group appears to be bound to iron through a monodentate interaction [20,28,29]. The Fe-O band may mask the S-S band due to overlapping ranges.

In the FTIR spectra of pure APTES (Figure S1 of the Supplementary information), the characteristic bands at 1072 cm^{-1} indicate the presence of the Si−O−Si stretching vibration. The amine-related groups are

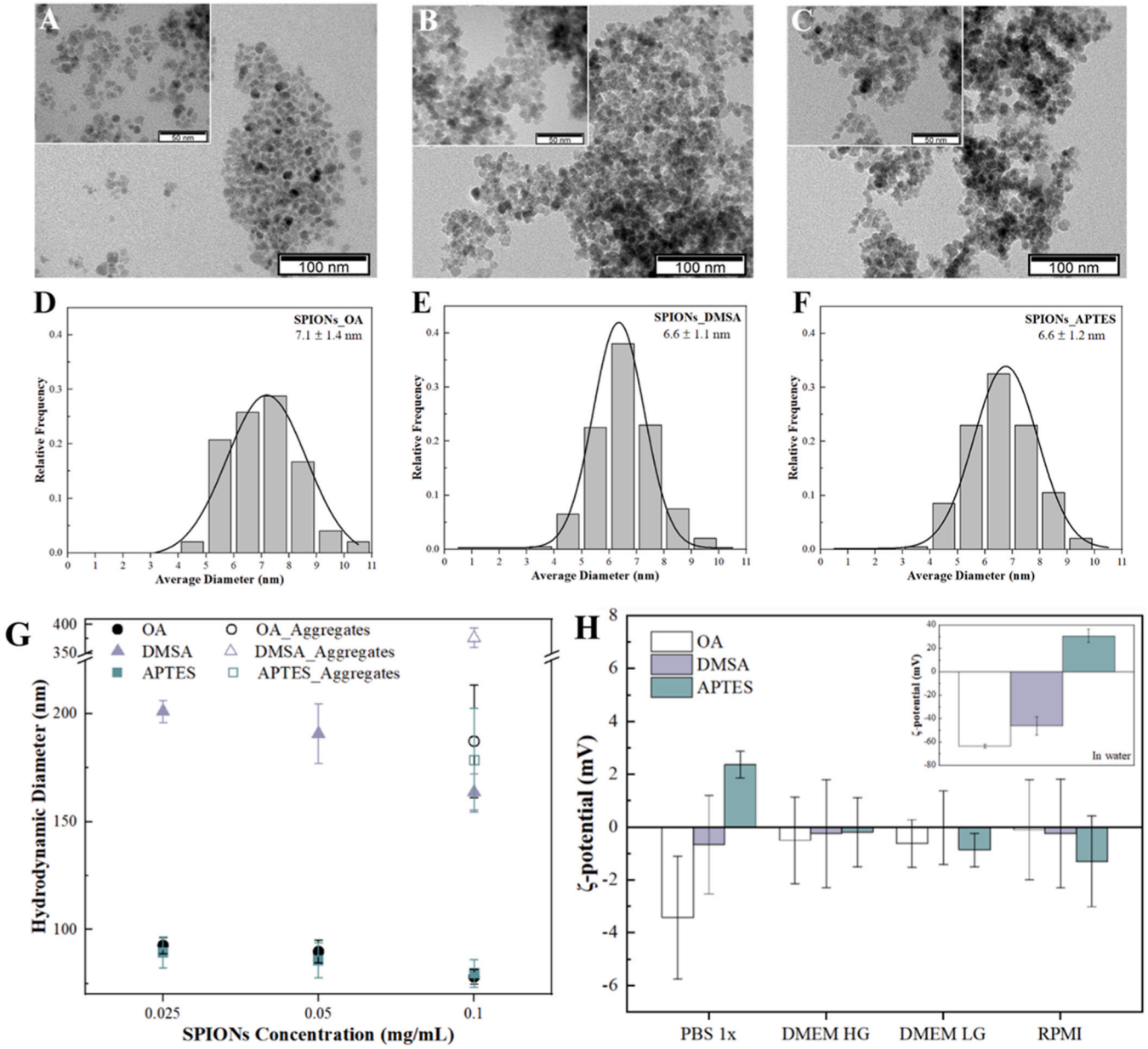

Fig. 2. TEM images and the corresponding size distribution graphs of SPIONs synthesized by chemical co-precipitation. OA-coated SPIONs (A, D), DMSA-coated SPIONs (B, E), and APTES-coated SPIONs (C, F). Scale bar of 50 nm (insets) and 100 nm. (G) Hydrodynamic diameter of SPIONs produced by chemical co-precipitation diluted in ultrapure water. SPIONs coated with OA (black), DMSA (purple), and APTES (green). Data is expressed as average ± standard deviation for at least five measurements. *(H)* ζ-potential analysis of SPIONs at 5 mg mL^{-1} in ultrapure water, PBS 1x, and cell culture media. SPIONs coated with OA (black), DMSA (purple), and APTES (green). Data is expressed as average ± standard deviation for at least three measurements.

present at 767 cm^{-1} (NH_2 bending vibration), 1166 cm^{-1} (C−N stretching vibration), and 1600 cm^{-1} (NH_2 scissoring of primary amines). Other characteristic bands are present at 1390 cm^{-1} (C−OH deformation vibration), 2884 cm^{-1} (CH_2 stretching vibration), 2974 and 2927 cm^{-1} (C−H stretching vibration) [30]. According to the literature, the primary mechanism behind the covalent anchoring of the aminopropyl silane groups is predominantly attributed to their self-polycondensation, which should be observed in a band at approximately 584 cm^{-1} [31]. However, the spectrum does not exhibit the presence of Fe-O-Si bonds, as these bands overlap with the Fe-O vibrations of the SPIONs. However, characteristic bands are present at approximately 1555 cm^{-1} (amine bending) and 959 cm^{-1} (Si-O stretching). The aliphatic chain is also present at 2860 and 2920 cm^{-1} [30].

The thermal stability of coated SPIONs was assessed by TGA, and the obtained curves are shown in Fig. 1 C. The OA-coated SPIONs display four distinct mass losses: up to 300°C (19.08 %), attributed to water desorption and removal of the free/weakly bound coating agent; 300–400°C (15.85 %) and 400–500°C (5.10 %), associated with decomposition of OA (indicating bilayer formation); and 500–890°C (11.07 %), likely from SPION weight loss due to gas production from the coating agent [32,33]. The significant difference in weight loss compared to DMSA and APTES-coated SPIONs can be attributed to inadequate freeze drying of the oil-based sample.

The DMSA-coated SPIONs exhibit two mass losses at ~200°C (5.14 %) and ~600°C (3.40 %), attributed to water loss and decomposition of DMSA ligands, respectively typically observed in three steps between 140 and 500 °C [34].

The APTES-coated SPIONs show a weight loss at ~200°C (1.32 %), likely due to water and impurities. Beyond this, APTES coating

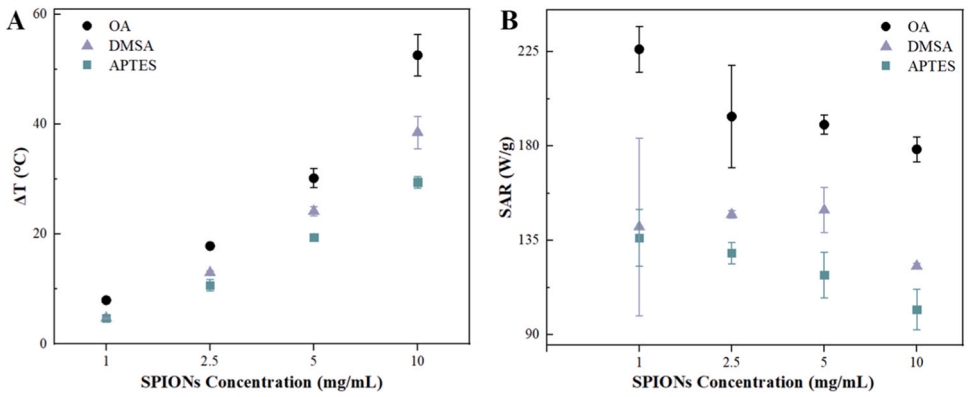

Fig. 3. Temperature variation (A) and SAR values (B) of SPIONs produced by chemical co-precipitation in ultrapure water for different concentrations and coatings. SPIONs coated with OA (black), DMSA (purple), and APTES (green). Temperature variation induced by applying an AMF with a 300 G intensity and a 388.4 kHz frequency for 10 min. Data is expressed as average ± standard deviation for at least three measurements.

decomposition leads to an additional weight loss of 4.98 % [35].

Magnetic measurements were performed to ensure that the produced SPIONs have superparamagnetic properties and to assess the effect of coating on the magnetic saturation. Fig. 1 D compares OA, DMSA, and APTES-coated SPIONs at 300 K. Magnetic saturation values are presented in A.m^2 per kilogram of the whole particle (including magnetic and non-magnetic material). Above the blocking temperature, all samples are superparamagnetic, determined by the absence of coercivity and remanence (inset of Fig. 1 D). The saturation magnetization (M_S) of OA SPIONs at 300 K is 44.0 A.m^2 kg^{-1}, while coating with APTES is 52.0 A.m^2 kg^{-1}, and with DMSA is 58.0 A.m kg^{-1}. Compared to pristine SPIONs evaluated elsewhere (58 A.m^2 kg^{-1} at 320 K) [5,20,21], the magnetic saturation is reduced with the coating molecules. This reduction is caused by coating, as previously observed [19,20]. When the saturation magnetization values are adjusted to A.m^2 per kg of magnetic core, the values increase to approximately 83 A.m^2 kg^{-1}, 60 A.m^2 kg^{-1}, and 53 A.m^2 kg^{-1} for OA, DMSA, and APTES-coated SPIONs respectively. These differences indicate that the influence of DMSA and APTES molecules on the saturation magnetization values is mainly dictated by the amount of coating molecules on the whole particle since the obtained values are close to those of pristine SPIONs [21]. In OA-coated SPIONs, a larger coating decreases particle aggregation, increasing the surface atoms-to-volume ratio, thus reducing the saturation magnetization value [18,36,37]. In addition, any anisotropy at the surface caused by non-homogeneous coating may affect the moment of the inner magnetic core via the exchange interaction with the outer surface [38]. The limitation of the Brownian relaxation mechanism can also reduce the saturation magnetization value [18].

3.2. Morphological analysis

TEM analysis was employed to examine the size, distribution, and morphology of synthesized SPIONs. Fig. 2 presents TEM images of OA (A and D), DMSA (B and E), and APTES (C and F) coated NPs, with average sizes of approximately 7.1 ± 1.4 nm, 6.6 ± 1.1 nm, and 6.6 ± 1.2 nm, respectively, all falling within a distribution range of 3–11 nm. All samples exhibit a high density of NPs per image, which may be caused by NP aggregation during sample preparation and solvent evaporation. All SPIONs exhibit a semi-spherical shape, which, according to the literature, can be attributed to the type of salts used for NP production or to the molar ratio of the iron ions [39]. The coatings did not impact core sizes, which remained between 6 and 8 nm, consistent with XRD findings.

3.3. Hydrodynamic size and zeta potential

Hydrodynamic size evaluation of synthesized SPIONs was conducted across three concentrations (0.025, 0.05, and 0.1 mg mL^{-1}). Fig. 2G illustrates the results. At 0.1 mg mL^{-1}, significant aggregate formation occurred across all NP types, rendering this concentration unsuitable for further measurements. At 0.025 mg mL^{-1}, OA, DMSA, and APTES-coated SPIONs exhibited sizes of approximately 93 nm, 201 nm, and 90 nm, respectively. Meanwhile, at 0.05 mg mL^{-1}, sizes were approximately 90 nm, 191 nm, and 86 nm for the same coatings, respectively, with slightly smaller sizes observed at this concentration. The hydrodynamic size of DMSA-coated nanoparticles is approximately double that obtained with the other two coating molecules. Therefore, we hypothesize that larger aggregates of nanoparticles are formed during the coating process, thus enlarging the final nanoparticle size. This is also visible in the TEM images, where larger aggregates are visible. Nevertheless, the zeta potential value is negative and within the stable range (30 mV in modulus) [40].

Additionally, the ζ-potential, crucial for colloidal system stability, was evaluated (Fig. 2 H). When the measurement was conducted in ultrapure water at a 0.05 mg mL^{-1} concentration, OA and DMSA-coated SPIONs displayed negative charges of −63.7 ± 1.5 mV and −46.3 ± 7.8 mV, respectively. APTES-coated SPIONs exhibited a positive charge of approximately + 30.5 ± 5.8 mV.

3.4. Magnetic hyperthermia measurements

The heat-producing capacity of SPIONs was assessed by exposing the samples to a magnetic field of 300 gauss and 388.4 kHz frequency. After a 30–40 sec stabilization period, the field was applied for 10 min. Four concentrations (1, 2.5, 5, and 10 mg mL^{-1}) were tested in ultrapure water, as shown in Figs. 3 and 4. Results depict variations among stabilizers, with OA-coated SPIONs exhibiting the highest ΔT and SAR values, while APTES-coated NPs showed the lowest. At 5 mg mL^{-1} concentration, ΔT values (in °C) were 30.2 ± 1.7, 24.2 ± 0.8, and 19.5 ± 0.6 for OA, DMSA, and APTES coatings, respectively. Corresponding SAR values (in W g^{-1}) were 190 ± 5, 149 ± 11, and 119 ± 11 for the same coatings and concentration. The selected concentration for subsequent tests was 5 mg mL^{-1}. Representative curves of the heating kinetics at 5 mg mL^{-1} are presented in Figure S2 of the Supplementary Information.

3.5. Stability evaluation of SPIONs during storage

Due to its significant role in determining the stability and behavior of colloidal systems, the ζ -potential of the different SPIONs was evaluated using different media [41]. As mentioned above, this parameter was first measured in ultrapure water, and the SPIONs coated with OA, DMSA, and APTES exhibited surface potentials (in mV) of −63.7 ± 1.5, −46.3 ± 7.8, and + 30.5 ± 5.8. However, in physiological conditions, protein

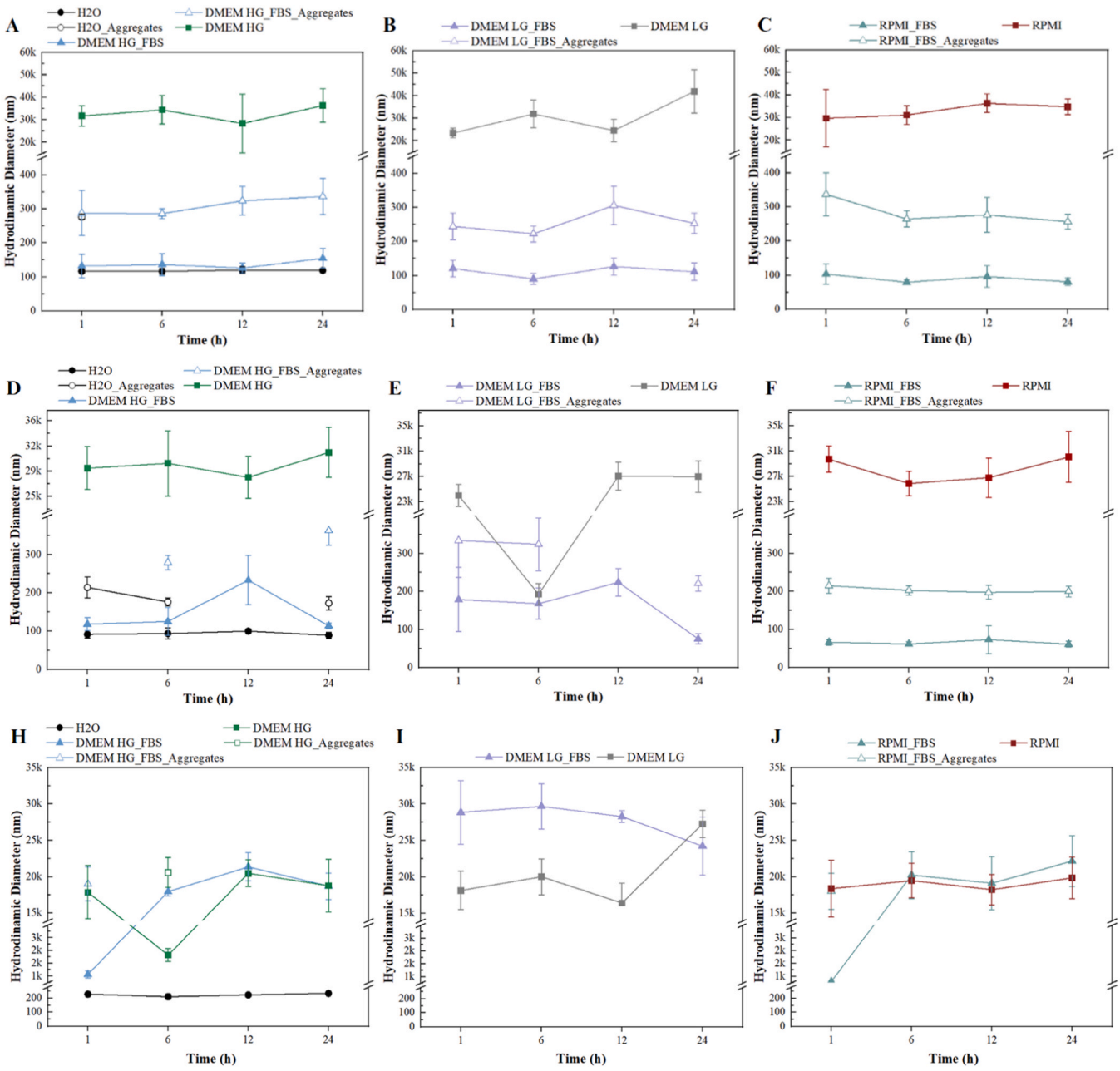

Fig. 4. Analysis of the dynamics of PC formation in coated SPIONs incubated for periods of 1 h, 6 h, 12 h, and 24 h at 0.05 mg mL^{-1} in different media. OA-coated SPIONs (A, B, C), DMSA-coated SPIONs (D, E, F) and APTES-coated SPIONs (H, I, J) ultrapure water and DMEM_HG with and without FBS (A, D, H), DMEM_LG with and without FBS (B, E, I) RPMI with and without FBS (C; F, J). Hydrodynamic diameter variation vs time. Data is expressed as average ± standard deviation for at least three measurements.

adsorption alters surface charge. Hence, ζ-potential was also analyzed in PBS 1x and cell culture media (DMEM-HG + 5 % FBS, DMEM-LG + 10 % FBS, and complete RPMI). Results in Fig. 2 H showed values closer to zero in PBS, with more pronounced effects in cell culture media.

To gain a deeper insight into PC formation in the SPIONs synthesized, the D_H was measured using the DLS technique. Testing involved ultrapure water as a control and three cell culture media related to the cell lines used, with and without FBS, across four-time intervals (1 h, 6 h, 12 h, and 24 h). Results for OA, DMSA, and APTES-coated SPIONs are depicted in Fig. 4.

The results show that protein adsorption occurs rapidly, resulting in minimal variation over the time periods studied. OA and DMSA-coated SPIONs exhibited similar behavior, with serum-free media leading to larger hydrodynamic sizes. APTES-coated SPIONs showed the largest sizes, suggesting FBS contains abundant negatively charged proteins. Larger hydrodynamic sizes seen in APTES-coated SPIONs align with previous studies, indicating a positive surface charge results in larger PCs [13,42]. Calatayud *et al.* [13] conducted a study that also revealed significant differences in the hydrodynamic size of NPs with distinct surface charges after a 24-hour incubation in a protein-rich cell medium. After this time, the group observed that NPs with a positive surface charge exhibited a hydrodynamic size of approximately 3000 nm, while NPs with a negative surface charge measured approximately 1500 nm. In a study by Portilla *et al.* [11], the group evaluated PC formation using SPIONs coated with APTES and DMSA, using DMEM for incubation with different time points. They observed that the maximum hydrodynamic size occurred after an incubation of 5–10 h (2455 nm for APTES-coated SPIONs and 209 nm for DMSA-coated SPIONs) and then decreased until

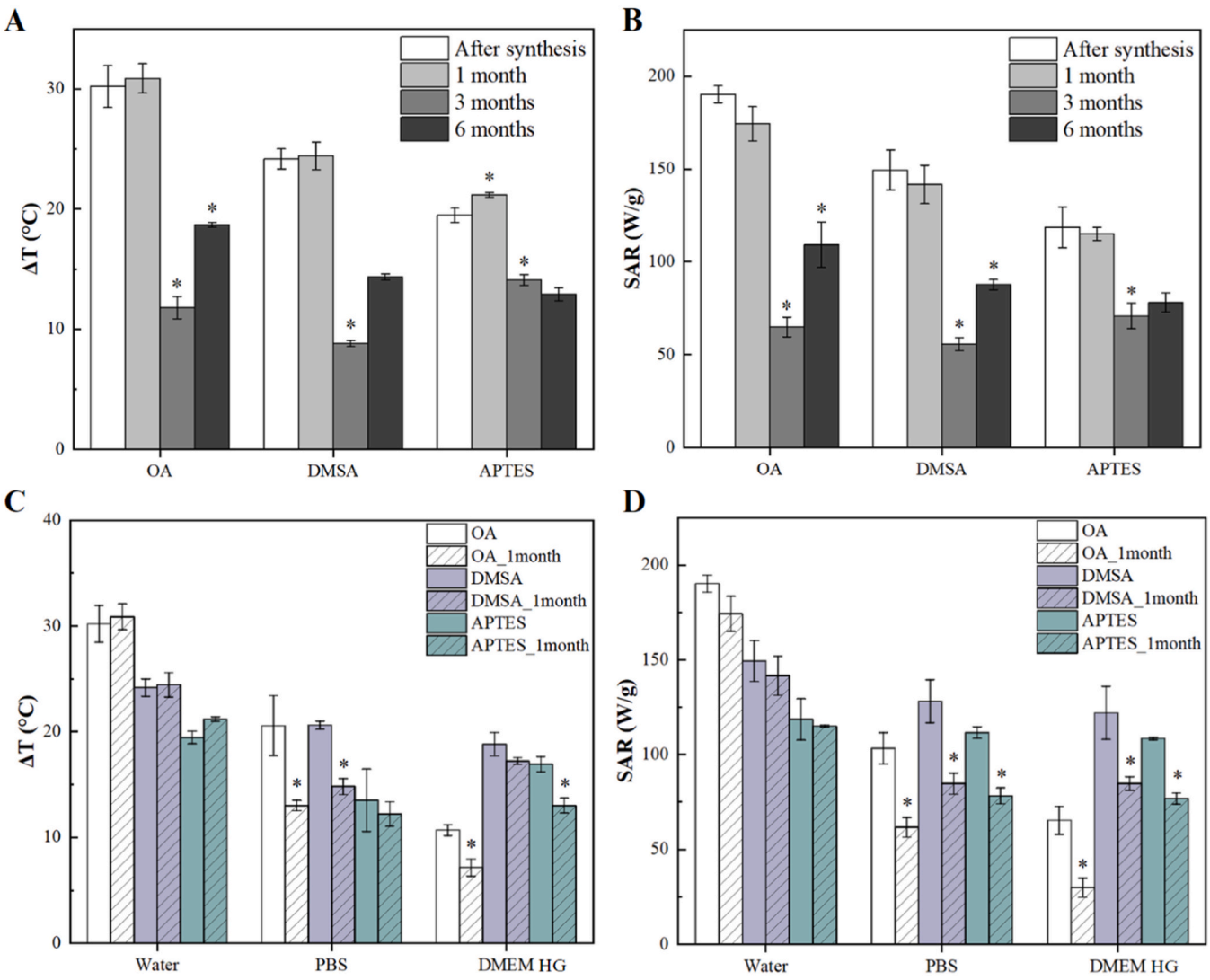

Fig. 5. Evaluation of SPIONs stability through analysis of temperature variation (A, C) and SAR values (B, D) over time. Evaluation of SPIONs stability at 5 mg mL^{-1} in ultrapure water (A, B), PBS 1x, and DMEM-HG + 10 % FBS (C, D). SPIONs coated with OA (white), DMSA (purple), and APTES (green). Temperature variation induced by applying an AMF with a 300 G intensity and a 388.4 kHz frequency for 10 min. Data is expressed as average ± standard deviation for at least three measurements. *p value < 0.05 compared with the previous measurement.

stabilizing after 24 h. While the sizes differed significantly from our study, the research group also noted a similar increase in the D_H of APTES-coated SPIONs, which is consistent with our findings.

ΔT and SAR values of SPIONs were measured at 1, 3, and 6 months post-synthesis to assess long-term stability. Samples, prepared at 5 mg mL^{-1} in ultrapure water, underwent the same field conditions as the initial characterization. Results are shown in Fig. 5A and B, with SAR values calculated using Eq. 1.

Significant differences were observed after 3 months, with a decrease in parameters in all types of SPIONs. In the case of temperature variation, this was approximately −18.40, −15.37, and −5.37 °C for SPIONs coated with OA, DMSA, and APTES, respectively. As for the SAR variation, for the same order of SPIONs it was approximately −125.27, −93.77, and −47.70 W g^{-1}. From this, we can see that the SPIONs coated with APTES showed the smallest decline. From 3–6 months, some increases in values were observed. In the case of temperature variation, this was approximately 6.90, 5.57, and −1.2 °C for the SPIONs coated with OA, DMSA, and APTES, respectively. The SAR variation for the same order of SPIONs was approximately 44.29, 32.09, and 7.26 W g^{-1}. The observed increase in values after 6 months may stem from challenges in maintaining consistent SPIONs concentration, likely due to increased aggregation and resistance to dispersion via sonication. Future investigations should include assessing hydrodynamic size over time to confirm aggregate formation. Kulikov *et al.* [43] observed a (smaller) decrease in SAR values after 18 months in OA-coated SPIONs, attributing it to alterations in magnetic properties resulting from the potential oxidation of Fe^{2+} ions in the Fe_3O_4 structure, consequently impacting the NPs' surface anisotropy. Ultimately, underscoring the significance of periodically monitoring physicochemical attributes of standard NPs, including size/agglomeration, surface charge, and, as illustrated in this context, heat capacity, throughout the study duration is crucial. Such monitoring allows any changes to be considered when interpreting and analyzing the collected data.

The heating capacity of SPIONs after 1 month was assessed in different solvents at a concentration of 5 mg mL^{-1} in ultrapure water, PBS, and DMEM-HG. Results in Fig. 5C and D showed a reduction in ΔT and SAR values, notably significant when PBS and DMEM-HG were used as dispersion media. The considerable reduction observed when DMEM-HG was utilized as dispersion media can be attributed to the formation of a PC, which enhances the propensity for aggregate formation.

The hydrodynamic diameter and zeta potential were also measured after one month of storage in different media to understand the

Table 1
Evaluation of SPIONs stability after one month of storage in water, PBS, and DMEM HG. The results are presented as the hydrodynamic diameter (D_H) and the aggregates (when present), the polydispersion index (PDI), and the Zeta potential. The measurements were performed after synthesis (48 h) and after 1 month. Data is expressed as average ± standard deviation for at least three measurements.

Sample	Medium		D_H (nm)	Aggregates (nm)	PDI	Zeta potential (mV)
OA	Water	After synthesis	89.8 ± 5.2	-	0.22 ± 0.04	−63.7 ± 1.5
		1 month	116 ± 3	-	0.22 ± 0.04	−85.5 ± 2.8
	PBS	After synthesis	168 ± 8	26797 ± 1869	0.49 ± 0.46	−3.43 ± 2.33
		1 month	141 ± 21	27398 ± 6459	1.9 ± 0.5	−14.0 ± 2.3
	DMEM HG	After synthesis	195 ± 27	464 ± 36	0.24 ± 0.06	−0.50 ± 1.6
		1 month	331 ± 12	17453 ± 1956	0.81 ± 0.07	−1.63 ± 1.45
DMSA	Water	After synthesis	191 ± 14	-	0.21 ± 0.06	−46.3 ± 7.8
		1 month	152 ± 9	288 ± 5	0.23 ± 0.04	−46.1 ± 1.5
	PBS	After synthesis	4043 ± 4010	18311 ± 1352	1.6 ± 0.5	−0.67 ± 1.9
		1 month	1530 ± 89	16119 ± 2589	1.2 ± 0.2	−9.73 ± 5.59
	DMEM HG	After synthesis	427 ± 107	19260 ± 4533	0.76 ± 0.16	−0.25 ± 2.05
		1 month	143 ± 47	306 ± 43	0.23 ± 0.06	+ 1.03 ± 2.46
APTES	Water	After synthesis	85.8 ± 8.1	-	0.19 ± 0.05	+ 30.5 ± 5.8
		1 month	153 ± 10	-	0.20 ± 0.04	+ 6.90 ± 1.48
	PBS	After synthesis	-	16575 ± 7661	1.9 ± 0.1	+ 2.37 ± 0.50
		1 month	1575 ± 95	16286 ± 1050	1.6 ± 0.2	−2.50 ± 0.60
	DMEM HG	After synthesis	-	23273 ± 1468	2.3 ± 0.2	−0.2 ± 1.3
		1 month	951 ± 42	17109 ± 2359	0.99 ± 0.09	+ 0.27 ± 2.12

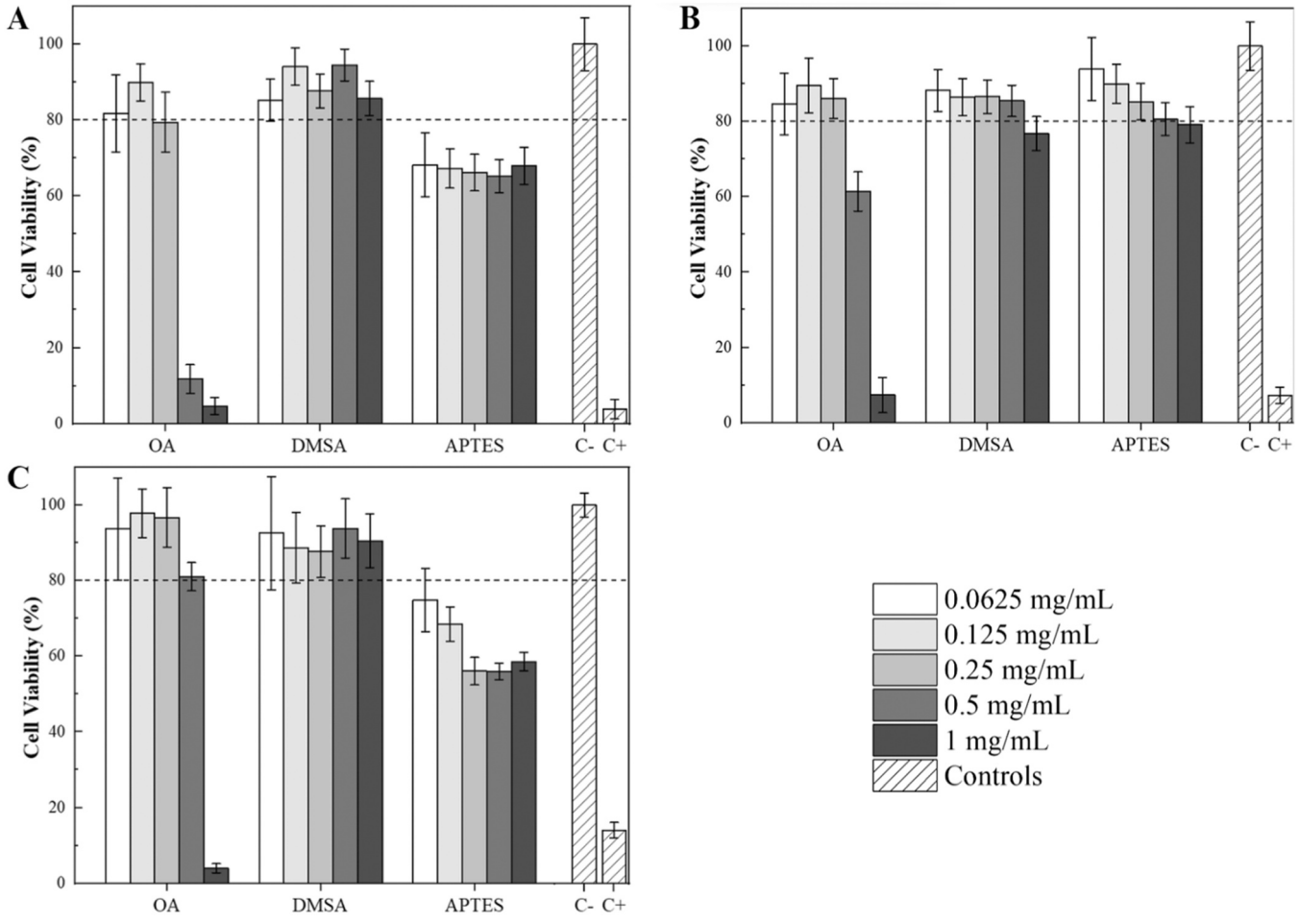

Fig. 6. Cell viability assay of the HFFF2 (A), WM983b (B), and THP-1 (C) cell lines after 24 h of incubation with the three types of SPIONs produced. Data is expressed as mean ± uncertainty for three independent experiments with five replicates for each condition.

evolution of the heating ability under storage (Table 1). It is visible that in water, OA appears to be the most stable coating molecule, as the DH exhibits a slight increase, with no significant effect on the zeta potential value. On the other hand, APTES exhibits an increase in the DH, with a substantial decrease in the zeta potential, which may indicate that this coating molecule does not confer a high stability over time.

When samples are stored in PBS, a significant increase in DH is observed, accompanied by a substantial decrease in the zeta potential value. This indicates that, in this media, the nanoparticles are not stable. Since the viscosity of PBS is very similar to water, thus not influencing

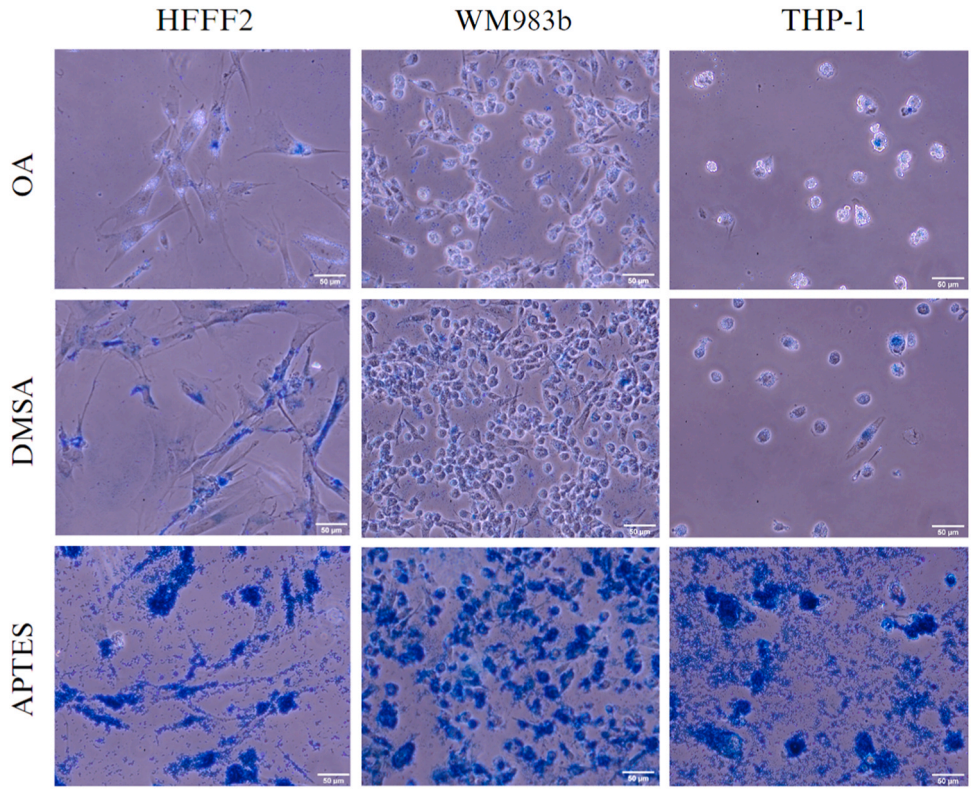

Fig. 7. SPIONs intracellular localization in the different cell types after staining with Prussian blue. HFFF2, WM983b, and THP-1 cells were incubated with 100 μg mL^{-1} of SPIONs coated with OA, DMSA, and APTES for 24 h. Brightfield images at 40x objective magnification with scale bar: 50 μm.

the DLS measurements [40], the most plausible explanation may be related to interactions between the coating molecule and the ions present in PBS. The major component of PBS is sodium chloride. These monovalent cations may interact with the carboxylic acid groups of oleic acid and DMSA, forming larger aggregates, thus significantly compromising the nanoparticles' stability [40,44]. In addition, the specific interaction of these ions with the coating molecule significantly affects the isoelectric point of the nanoparticle, dramatically affecting the zeta potential value at pH 7.4.

In DMEM HG, all samples exhibit the propensity to form larger aggregates, which may be explained by protein corona formation, as previously demonstrated (Fig. 4).

3.6. *In vitro analysis*

3.6.1. *Cytotoxicity study*

Since SPIONs hold great promise as candidates for MH applications, which involve direct contact with the human body, their biocompatibility is of utmost importance. Thus, SPIONs were evaluated for cytotoxicity towards HFFF2 (Figs. 6–8A), WM983b (Fig. 8 B), and THP-1 cell lines (Fig. 8C) using the resazurin colorimetric method. Cells were exposed to different concentrations of NPs for 24 h. The results are expressed as the percentage of cell viability relative to the negative control (cells not exposed to NPs but maintained under the same conditions). SPIONs concentrations that resulted in a cell viability above 80 % were considered non-cytotoxic.

The results showed non-cytotoxicity at lower concentrations for OA-coated SPIONs, while DMSA-coated SPIONs exhibited the lowest overall cytotoxicity. Conversely, SPIONs coated with APTES exhibited moderate cytotoxicity in fibroblast and macrophage cell lines. The behavior did not appear to be dose-dependent, remaining relatively constant as the concentration of NPs increased. A Live/Dead assay was also performed (results presented in Figure S3 in the Supplementary Materials section), revealing that there appears to be no direct correlation between cell viability and the NP concentration used. Furthermore, the resazurin assay was also performed after 48 h of cell exposure to the SPIONs synthesized, but as can be seen in Figure S4 in the Supplementary Materials section, no significant differences were observed after this period; thus, subsequent assays were conducted at 24 h.

3.6.2. *Internalization study*

Images of the interaction of SPIONs with the HFFF2, WM983b, and THP-1 cell lines, determined by Prussian blue staining, were captured after 1 h, 6 h, and 24 h of exposure (Figures S5, S6, and S7 in the Supplementary Material). Fig. 7 presents the images captured after 24 h.

Increasing blue color intensity over time indicates higher NPs presence on cell membranes or internalization. APTES-coated SPIONs showed greater intracellular uptake, followed by DMSA-coated SPIONs and OA-coated SPIONs. Macrophages exhibited enhanced internalization, particularly within the first hour. Fibroblasts showed higher internalization than melanoma cells. This result is consistent with the literature, suggesting positively charged NPs are more efficiently internalized due to electrostatic attraction with negatively charged cell membranes [45]. This electrostatic attraction is generally considered a primary driving force in regulating the cellular uptake of NPs [45]. Calatayud *et al.* [13] investigated the impact of surface charge on hydrodynamic size when exposed to physiological media and the influence of this charge on NP internalization in neuroblastoma cells. According to their work, positively charged NPs were fully incorporated by cells, while less than 50 % of negatively charged NPs were absorbed. Additionally, DMSA-coated SPIONs show relatively higher internalization than OA-coated ones, likely due to their lower negative charge and smaller hydrodynamic size, facilitating cell absorption. Finally, an enhanced internalization of SPIONs by macrophages, especially within the first hour of exposure, is observed. While the uptake mechanism is unclear, some SPIONs are studied as nuclear magnetic resonance (NMR) markers for diseases linked to high macrophage activity [46,47]. Furthermore, a noticeable difference in internalization can be observed

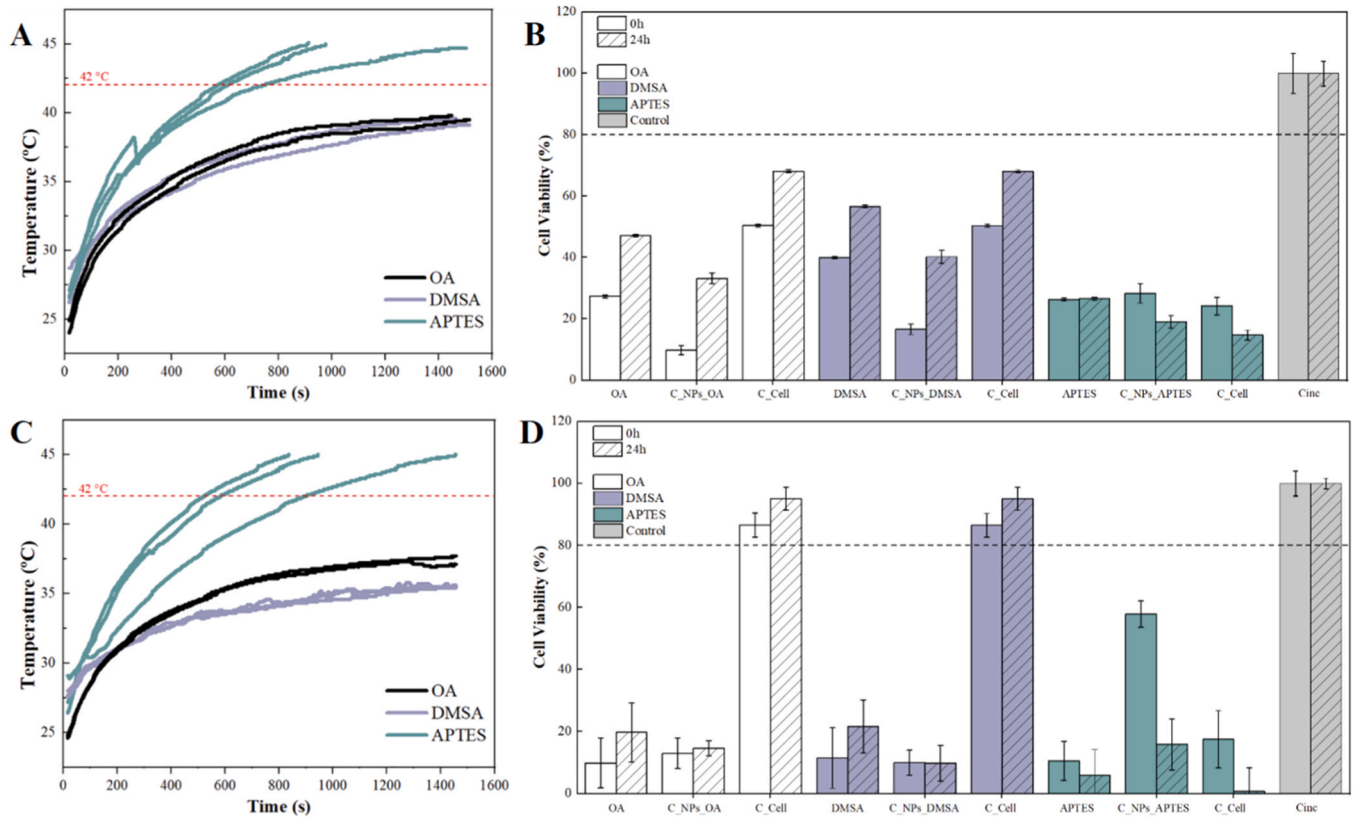

Fig. 8. *In vitro* MH (A, C) and subsequent cell viability assays (B, D) of HFFF2 fibroblasts (A, B) and WM983b melanoma cells (C, D) incubated for 24 h with the different types of SPIONs. SPIONs coated with OA (black), DMSA (purple), and APTES (green). Temperature variation was induced by applying an AMF with a 300 G intensity and a 388.4 kHz frequency until a temperature of 45 °C or until 25 min of heating was reached. Two replicates are presented for OA- and DMSA-coated SPIONs, and three replicates for the APTES-coated SPIONs. The cell viability test was carried out immediately after the MH test (0 h) and 24 h after (24 h). "C_NPs_X" denotes the NPs control (unheated vial with SPIONs and cells), X being OA, APTES, or DMSA, "C_Cell" denotes the unheated Cell controls (without NPs) that accompanied the vials to be measured, and finally, "Cinc" (gray bars) denotes a cell control (without NPs) kept in the incubator. Cell viability was calculated as a percentage of the cell control (incubated), and data is expressed as mean ± uncertainty for at least five replicas for each condition.

between the HFFF2 and WM983b cell lines, with fibroblasts exhibiting a higher internalization rate than the melanoma cell line. This finding is particularly noteworthy, as recent studies indicate that extracellular MH results in elevated levels of cell apoptosis due to the higher heating efficiency of SPIONs. For example, Hannon *et al.* [48] observed extracellular hyperthermia causing significant necrosis in pancreatic cancer cells, while intracellular hyperthermia did not impact viability. In another study, it was demonstrated that SAR values were higher when SPIONs were in the extracellular environment, and consequently, inhibiting the cellular uptake of SPIONs enhances the efficacy of MH [49].

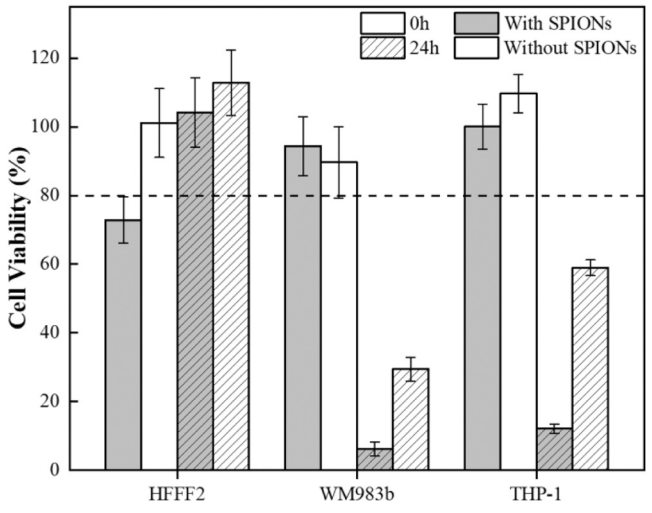

Fig. 9. Cell viability of the three cell lines (HFFF2, WM983b, and THP-1) after 1 h of sand bath hyperthermia (42–44 °C). Viability was tested right after heating and after a 24-hour incubation period. The influence of exposure to 100 μg mL^{-1} of APTES-coated SPIONs during 24 h of pre-warming incubation was also tested. The percentage of cell viability was calculated as a percentage to incubated cell controls (not exposed to either heat or SPIONs), and the data are expressed as mean ± uncertainty for at least five replicates for each condition.

3.6.3. *In vitro magnetic hyperthermia*

MH assays were initially performed in Petri dishes to enhance cell adhesion. However, the temperatures achieved were below the desired levels, peaking at 30.7 °C, as demonstrated in Figure S8 in the Supplementary Materials section. The 2D heating attempts proved insufficient for reaching physiological temperatures. Therefore, further MH tests were conducted in hyperthermia flasks to optimize parameters.

The results of the MH tests using different types of SPIONs with the HFFF2 and WM983b cell lines are shown in Fig. 8 (A and C, respectively). Abrupt temperature changes in the temperature curves can be attributed to SPION sedimentation during measurement. Only APTES-coated SPIONs achieved the desired temperatures, with faster heating observed in melanoma cells. DMSA-coated SPIONs reached maximum temperatures of 39.2 °C (HFFF2) and 35.6 °C (WM983b), while OA-coated SPIONs peaked at 39.8 °C (HFFF2) and 37.7 °C (WM983b). The temperature difference between cell lines may stem from increased aggregation and precipitation observed in WM983b flasks, contrasting

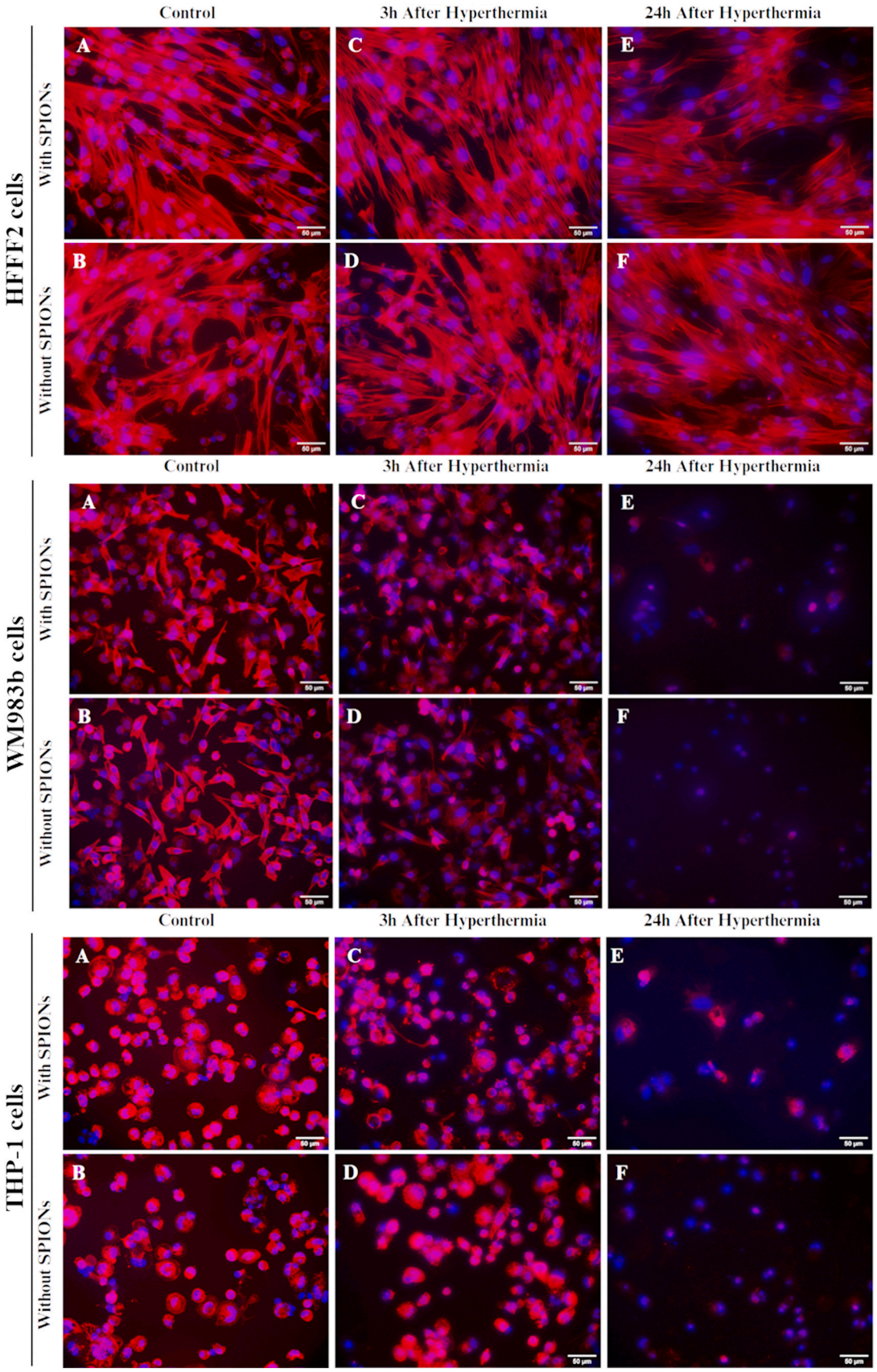

Fig. 10. Fluorescence images of cells stained with phalloidin (F-actin filaments in red) and DAPI (nucleus in blue) 3 h and 24 h after sand bath hyperthermia. The influence of exposure to 100 µg mL^{-1} of APTES-coated SPIONs during 24 h of pre-heating incubation was also tested. Unheated control cells are shown in the first column (A, B). Scale bar: 50 µm.

with the more stable conditions in HFFF2 flasks.

Resazurin assays conducted post-MH (0 h) immediately and after 24 h, shown in Fig. 8 (B and D), demonstrate a notable decline in viability, especially pronounced in WM983b cells. Fibroblast viability post-assay using OA and DMSA-coated SPIONs showed partial recovery after 24 h. Reduced viability in both cell and SPION controls may result from NP cytotoxicity and suboptimal assay conditions (e.g., challenging to maintain sterility). Interestingly, fibroblast viability showed signs of recovery 24 h post-assay, especially when subjected to hyperthermia using OA and DMSA-coated SPIONs.

In summary, APTES-coated SPIONs induced a more significant viability reduction, correlating with higher temperatures achieved and consistent with the melanoma cell line's heightened susceptibility, as reported in the literature [50]. Further evaluation at 48 h could provide insights into the evolving behavior of both melanoma cells and fibroblasts.

Due to the challenges encountered while attempting to detach cells from the hyperthermia flasks for subsequent assays, a sand bath was employed to simulate temperature rising within the therapeutic range. In this procedure, cells from the three cell lines were individually seeded in a 24-well plate, allowed to adhere, and then exposed to 100 μg mL^{-1} of APTES-coated SPIONs. Following a 24-hour incubation period, the plate was subjected to a sand bath for 1 h, maintaining a temperature range of 42–44 °C. The results of the subsequent resazurin assays, normalized to a control group not subjected to either SPIONs or temperature, are depicted in Fig. 9. These outcomes demonstrate that the fibroblast cell line was the least affected by heating, while the melanoma cell line exhibited the most pronounced impact. It was also possible to observe that the presence of SPIONs led to a more significant decrease in viability, even though it was not a MH assay. This can be justified by some possible cytotoxicity and the fact that SPIONs are good heat conductors since they are NPs composed of iron oxide.

As previously mentioned, the precise mechanism driving cell death resulting from hyperthermia remains a subject of ongoing research. This lack of consensus arises due to the multitude of parameters that, when altered, activate diverse cell death pathways. Existing literature indicates that numerous cell lines exhibit limited tolerance towards temperatures around 44 – 45 °C. This has various detrimental effects, including increased apoptosis or necrosis-associated cell death. This phenomenon is observed across multiple cell types, such as human erythroleukemia cells, murine melanoma cells, and prostate stromal cells [51–54]. However, some lines have been shown to resist this treatment, such as the RIF-1 line and osteosarcoma [55,56]. This may be because cancer cells usually have a poor apoptosis regulation system; for example, Yonezawa *et al.* [56] found a direct transition to necrosis at 44 °C. Additionally, some cell lines initially display short-term heat shock tolerance but subsequently experience reduced viability, as seen in melanoma (Bowes) cells and lung adenocarcinoma cells [54,57].

The response of cytoskeletal structure to heat shock also varies widely depending on factors such as cell type, attained temperature, and duration of heating. Prasad *et al.* [58] observed that Hela cells demonstrated different degrees of membrane blebbing following hyperthermia treatment, accompanied by notable disruption of actin and tubulin cytoskeletons. This disruption was posited as a potential cause of cell death following hyperthermia treatment. In a study by Garcia *et al.* [54], acute and long-term impacts of hyperthermia (45 °C, 30 min, in a water bath) on the B16-F10 murine melanoma cell line were investigated. Immediate harmful effects were observed post-heating, with diminished peripheral F-actin (filamentous actin) rings after 3 h and altered F-actin cytoskeleton, loss of cell boundaries, cell shrinkage, and nuclear material condensation after 24 h. Additional effects encompassed disruption of cell layer organization, intercellular contact, and a substantial reduction in attached cell count.

Following the resazurin assay, cells were fixed at 3- and 24-hours post-hyperthermia treatment, permeabilized, and stained using ActinstainingTM 555 Phalloidin Red and DAPI. Samples were visualized via an epi-fluorescence microscope, with results presented for fibroblast, melanoma, and macrophage cell lines in Fig. 10. The outcomes aligned with the resazurin assays, highlighting a reduction in viability, particularly within the WM983b cell line. Additionally, the definition and intensity of the actin filament-marking fluorophore were reduced. After 24 h, a comprehensive disruption of actin filaments was apparent, with only a few nuclei stained by DAPI. This correlates with the substantial decrease in cell viability previously noted. Actin cytoskeleton cleavage and disruption are frequently observed during apoptosis [14,15,59].

The decrease in cell viability over time also supports the hypothesis that the cytoskeletons of the treated cells were disrupted, thereby triggering the initiation of a signal leading to cell death. While some features described in the literature, such as loss of cell boundaries, cellular shrinkage, cytoplasmic contraction, and nuclear material condensation, were not evident in the images presented, these observations should be further explored [54,56]. Furthermore, marking microtubules could provide insight, as they are reported to be more sensitive to hyperthermia [58]. Given the anticipated generation of deleterious substances like free radicals and ROS due to elevated temperatures, assessing their formation could offer valuable insights into cellular stress [60].

4. Conclusions

In conclusion, this study elucidates the significant potential of SPIONs for MH cancer therapy. Our exploration of different SPION coatings, namely OA, DMSA, and APTES, has provided valuable insights into their respective efficacy. All samples retained most of their heating capacity during 1-month storage. APTES-coated SPIONs exhibited enhanced internalization in melanoma cells compared to the negatively charged SPIONs. In magnetic hyperthermia measurements, APTES-coated SPIONs achieved therapeutic temperatures, leading to a significant decrease in melanoma cell viability upon application of an AMF. Our study highlights the potential of APTES-coated SPIONs for cancer therapy. It emphasizes the importance of tailored coatings and the need for ongoing research to unlock the therapeutic potential of SPION-based MH fully. The complex interplay between SPIONs and biological systems demands continued exploration to pave the way for future advancements in this promising field.

Declaration of Competing Interest

The authors declare the following financial interests/personal relationships which may be considered as potential competing interests: Paula Soares reports financial support was provided by NOVA University Lisbon NOVA School of Science & Technology. Paula Soares reports article publishing charges, equipment, drugs, or supplies, and travel were provided by Foundation for Science and Technology. Paula Soares reports a relationship with NOVA University Lisbon NOVA School of Science & Technology that includes: employment. If there are other authors, they declare that they have no known competing financial interests or personal relationships that could have appeared to influence the work reported in this paper.

Acknowledgments

This work was financed by FCT—Portuguese Foundation for Science and Technology, in the framework of the project PTDC/BTM-MAT/2472/2021 and projects LA/P/0037/2020, UIDP/50025/2020 and UIDB/50025/2020 of the Associate Laboratory Institute of Nanostructures, Nanomodelling and Nanofabrication-i3N. The authors also acknowledge the support of FCT-Fundação para a Ciência e a Tecnologia, I.P. in the scope of project 2022.07258.PTDC.

Appendix A. Supporting information

Supplementary data associated with this article can be found in the

online version at doi:10.1016/j.nxnano.2025.100141.

References

[1] World Health Organization, Cancer. [cited 2023 Aug 23]; Available from: https://www.who.int/en/news-room/fact-sheets/detail/cancer.
[2] *Globocan 2022*. December 2, 2024; Available from: ⟨https://gco.iarc.fr/today/data/factsheets/cancers/39-All-cancers-fact-sheet.pdf⟩.
[3] F. Bray, et al., The ever-increasing importance of cancer as a leading cause of premature death worldwide, Cancer 127 (16) (2021) 3029–3030.
[4] K. Wu, et al., Magnetic nanoparticles in nanomedicine: a review of recent advances, Nanotechnology 30 (50) (2019) 502003.
[5] P.I.P. Soares, et al., Iron oxide nanoparticles stabilized with a bilayer of oleic acid for magnetic hyperthermia and MRI applications, Appl. Surf. Sci. 383 (2016) 240–247.
[6] M. Rahman, et al., Biomedical applications of superparamagnetic nanoparticles in molecular scale, Curr. Org. Chem. 19 (11) (2015) 982–990.
[7] X. Liu, et al., Comprehensive understanding of magnetic hyperthermia for improving antitumor therapeutic efficacy, Theranostics 10 (8) (2020) 3793–3815.
[8] Chaparro, C.I.P., et al. Application of Hyperthermia for Cancer Treatment: Synthesis and Characterization of Magnetic Nanoparticles and their internalization on Tumor Cell Lines*. in 2019 IEEE 6th Portuguese Meeting on Bioengineering (ENBENG). 2019.
[9] K. Nienhaus, G.U. Nienhaus, Mechanistic understanding of protein corona formation around nanoparticles: old puzzles and new insights, Small 19 (28) (2023) e2301663.
[10] G. Bashiri, et al., Nanoparticle protein corona: from structure and function to therapeutic targeting, Lab a Chip 23 (6) (2023) 1432–1466.
[11] Y. Portilla, et al., Iron oxide nanoparticle coatings dictate cell outcomes despite the influence of protein coronas, ACS Appl. Mater. Interfaces 13 (7) (2021) 7924–7944.
[12] C. Guibert, et al., Hyperthermia of magnetic nanoparticles: experimental study of the role of aggregation, J. Phys. Chem. C. 119 (50) (2015) 28148–28154.
[13] M.P. Calatayud, et al., The effect of surface charge of functionalized Fe3O4 nanoparticles on protein adsorption and cell uptake, Biomaterials 35 (24) (2014) 6389–6399.
[14] Y. Li, et al., Mechanical stretching induces fibroblasts apoptosis through activating Piezo1 and then destroying actin cytoskeleton, Int J. Med Sci. 20 (6) (2023) 771–780.
[15] S.M. Laster, J.M. Mackenzie Jr., Bleb formation and F-actin distribution during mitosis and tumor necrosis factor-induced apoptosis, Microsc. Res Tech. 34 (3) (1996) 272–280.
[16] P. Clerc, et al., Targeted magnetic intra-lysosomal hyperthermia produces lysosomal reactive oxygen species and causes caspase-1 dependent cell death, J. Control Release 270 (2018) 120–134.
[17] L. Beola, et al., The intracellular number of magnetic nanoparticles modulates the apoptotic death pathway after magnetic hyperthermia treatment, ACS Appl. Mater. Interfaces 12 (39) (2020) 43474–43487.
[18] P.I. Soares, et al., Thermal and magnetic properties of iron oxide colloids: influence of surfactants, Nanotechnology 26 (42) (2015) 425704.
[19] P.I. Soares, et al., Thermal and magnetic properties of chitosan-iron oxide nanoparticles, Carbohydr. Polym. 149 (2016) 382–390.
[20] R.J.R. Matos, et al., Electrospun composite cellulose acetate/iron oxide nanoparticles non-woven membranes for magnetic hyperthermia applications, Carbohydr. Polym. 198 (2018) 9–16.
[21] P.I. Soares, et al., Effects of surfactants on the magnetic properties of iron oxide colloids, J. Colloid Interface Sci. 419 (2014) 46–51.
[22] M. Talelli, et al., Superparamagnetic iron oxide nanoparticles encapsulated in biodegradable thermosensitive polymeric micelles: toward a targeted nanomedicine suitable for image-guided drug delivery, Langmuir 25 (4) (2009) 2060–2067.
[23] N. Fauconnier, et al., Thiolation of maghemite nanoparticles by dimercaptosuccinic acid, J. Colloid Interface Sci. 194 (2) (1997) 427–433.
[24] M.H. Mashhadizadeh, M. Amoli-Diva, Drug-carrying amino silane coated magnetic nanoparticles as potential vehicles for delivery of antibiotics, J. Nanomed. Nanotechnol. (2012) 03.
[25] P.I.P. Soares, et al., Effects of surfactants on the magnetic properties of iron oxide colloids, J. Colloid Interface Sci. 419 (2014) 46–51.
[26] A. Aliakbari, et al., Influence of different synthesis conditions on properties of oleic acid-coated-Fe3O4 nanoparticles, Mater. Sci. -Pol. 33 (1) (2015) 100–106.
[27] K. Winiarczyk, et al., Magnetic properties of iron oxide nanoparticles with a DMSA-modified surface, Hyperfine Interact. 242 (1) (2021) 48.
[28] E.S. Martins, et al., Potential use of DMSA-containing iron oxide nanoparticles as magnetic vehicles against the COVID-19 disease, ChemistrySelect 6 (31) (2021) 7931–7935.
[29] S.I. Palma, et al., Effects of phase transfer ligands on monodisperse iron oxide magnetic nanoparticles, J. Colloid Interface Sci. 437 (2015) 147–155.
[30] S. Mohapatra, et al., A simple synthesis of amine-derivatised superparamagnetic iron oxide nanoparticles for bioapplications, J. Mater. Sci. 42 (17) (2007) 7566–7574.
[31] X.-Y. Wang, et al., Optimizing the silanization of thermally-decomposed iron oxide nanoparticles for efficient aqueous phase transfer and MRI applications, RSC Adv. 6 (96) (2016) 93784–93793.
[32] F. Senturk, S. Cakmak, G. Guler Ozturk, Synthesis and characterization of oleic acid coated magnetic nanoparticles for hyperthermia applications, Nat. Appl. Sci. J. 2 (2) (2019) 16–29.
[33] K. Petcharoen, A. Sirivat, Synthesis and characterization of magnetite nanoparticles via the chemical co-precipitation method, Mater. Sci. Eng.: B 177 (5) (2012) 421–427.
[34] S. Çitoğlu, et al., DMSA-coated cubic iron oxide nanoparticles as potential therapeutic agents, Nanomedicine 16 (11) (2021) 925–941.
[35] L.M. Al-Harbi, M.S.A. Darwish, Functionalized iron oxide nanoparticles: synthesis through ultrasonic-assisted co-precipitation and performance as hyperthermic agents for biomedical applications, Heliyon 8 (6) (2022) e09654.
[36] L. Garcell, et al., Interfacial and rheological characteristics of maghemite aqueous suspensions, J. Colloid Interface Sci. 205 (2) (1998) 470–475.
[37] A.P. Philipse, M.P.B. Vanbruggen, C. Pathmamanoharan, Magnetic silica dispersions - preparation and stability of surface-modified silica particles with a magnetic core, Langmuir 10 (1) (1994) 92–99.
[38] Zeng, L., et al. Preparation and Characterization of Amino-Coated Maghemite Nanoparticles. in 2010 4th International Conference on Bioinformatics and Biomedical Engineering. 2010.
[39] A.K. Gupta, M. Gupta, Synthesis and surface engineering of iron oxide nanoparticles for biomedical applications, Biomaterials 26 (18) (2005) 3995–4021.
[40] S. Bhattacharjee, DLS and zeta potential - what they are and what they are not? J. Control Release 235 (2016) 337–351.
[41] D.J. Pochapski, et al., Zeta potential and colloidal stability predictions for inorganic nanoparticle dispersions: effects of experimental conditions and electrokinetic models on the interpretation of results, Langmuir 37 (45) (2021) 13379–13389.
[42] U. Sakulkhu, et al., Significance of surface charge and shell material of superparamagnetic iron oxide nanoparticle (SPION) based core/shell nanoparticles on the composition of the protein corona, Biomater. Sci. 3 (2) (2015) 265–278.
[43] O.A. Kulikov, et al., Magnetic hyperthermia nanoarchitectonics via iron oxide nanoparticles stabilised by oleic acid: anti-tumour efficiency and safety evaluation in animals with transplanted carcinoma, Int J. Mol. Sci. 23 (8) (2022).
[44] J. Lim, et al., Characterization of magnetic nanoparticle by dynamic light scattering, Nanoscale Res Lett. 8 (1) (2013) 381.
[45] D. Zhang, et al., The morphology and surface charge-dependent cellular uptake efficiency of upconversion nanostructures revealed by single-particle optical microscopy, Chem. Sci. 9 (23) (2018) 5260–5269.
[46] A.M.M. Dias, et al., Superparamagnetic iron oxide nanoparticles for immunotherapy of cancers through macrophages and magnetic hyperthermia, Pharmaceutics 14 (11) (2022).
[47] C. Polasky, et al., Impact of superparamagnetic iron oxide nanoparticles on THP-1 monocytes and monocyte-derived macrophages, Front Mol. Biosci. 9 (2022) 811116.
[48] G. Hannon, et al., Comparing the effects of intracellular and extracellular magnetic hyperthermia on the viability of BxPC-3 cells, Nanomater. (Basel) 10 (3) (2020).
[49] R. Di Corato, et al., Magnetic hyperthermia efficiency in the cellular environment for different nanoparticle designs, Biomaterials 35 (24) (2014) 6400–6411.
[50] A. Hervault, N.T. Thanh, Magnetic nanoparticle-based therapeutic agents for thermo-chemotherapy treatment of cancer, Nanoscale 6 (20) (2014) 11553–11573.
[51] L. Sharif-Khatibi, et al., Hyperthermia induces differentiation without apoptosis in permissive temperatures in human erythroleukaemia cells, Int J. Hyperth. 23 (8) (2007) 645–655.
[52] R.S. Oliveira Filho, R.G. Bevilacqua, R. Chammas, Hyperthermia increases the metastatic potential of murine melanoma, Braz. J. Med Biol. Res 30 (8) (1997) 941–945.
[53] M. Brehmer, I. Svensson, Heat-induced apoptosis in human prostatic stromal cells, BJU Int 85 (4) (2000) 535–541.
[54] M.P. Garcia, J.R. Cavalheiro, M.H. Fernandes, Acute and long-term effects of hyperthermia in B16-F10 melanoma cells, PLoS One 7 (4) (2012) e35489.
[55] R. Jayasundar, et al., Simultaneous evaluation of the effects of RF hyperthermia on the intra- and extracellular tumor pH, Magn. Reson Med 43 (1) (2000) 1–8.
[56] M. Yonezawa, et al., Hyperthermia induces apoptosis in malignant fibrous histiocytoma cells in vitro, Int J. Cancer 66 (3) (1996) 347–351.
[57] H. Fukao, et al., Effect of hyperthermia on the viability and the fibrinolytic potential of human cancer cell lines, Clin. Chim. Acta 296 (1-2) (2000) 17–33.
[58] N.K. Prasad, et al., Mechanism of cell death induced by magnetic hyperthermia with nanoparticles of γ-MnxFe2–xO3 synthesized by a single step process, J. Mater. Chem. 17 (48) (2007) 5042–5051.
[59] M. Desouza, P.W. Gunning, J.R. Stehn, The actin cytoskeleton as a sensor and mediator of apoptosis, Bioarchitecture 2 (3) (2012) 75–87.
[60] K. Ahmed, et al., Hyperthermia and protein homeostasis: cytoprotection and cell death, J. Therm. Biol. 91 (2020) 102615.